PCCP

ROYAL SOCIETY OF CHEMISTRY

PAPER

View Article Online
View Journal | View Issue

Cite this: *Phys. Chem. Chem. Phys.*, 2020, **22**, 13680

Two-dimensional tetragonal transition-metal carbide anodes for non-lithium-ion batteries†

Changcheng Ke,‡ Dong Fan, ‡ Chengke Chen, Xiao Li, Meiyan Jiang and Xiaojun Hu *

Received 14th February 2020,
Accepted 21st May 2020

DOI: 10.1039/d0cp00839g

rsc.li/pccp

Searching for high-performance anode materials with high energy-density, fast kinetics, and good stability is a key challenge for non-lithium-ion batteries (NLIBs), such as Na^+, K^+, Mg^{2+}, Ca^{2+}, Zn^{2+} and Al^{3+} ion batteries. Here, we systematically investigated the performance of a new class of two-dimensional tetragonal transition-metal carbides (tetr-MCs) using first-principles calculations, as anodes for NLIBs. The results show that tetr-MCs are ideal anode materials with good stabilities, favorable mechanical properties, intrinsic metallic properties, high theoretical capacities, and fast ion diffusion rate for NLIBs. Among all tetr-MCs, we found that the energy barrier of Mg atoms on tetr-TiC is only 54 meV and that of Al atoms on tetr-VC is 101 meV, which are lower than the energy barriers of 230–500 meV of the well-studied MXenes, indicating that tetr-VC and tetr-TiC monolayers are promising anodes for NLIBs. Therefore, compared to MXenes, tetr-MCs show many advantages for NLIB applications, such as a lower diffusion barrier (minimum 54 meV), a high theoretical capacity (up to 1450 mA h g^{-1}), and a lower average open circuit voltage (0.05–0.77 V). The results are of great significance for the experimental preparation of excellent anode materials for NLIBs.

1. Introduction

Lithium-ion batteries (LIBs) have been widely used in small electronic devices such as mobile phones, notebook computers, *etc.* due to their high energy density, high operating voltage, excellent cycling performance, and environmental friendliness.[1,2] In recent years, as the performance of rechargeable LIBs has been continuously improved, the application range of LIBs has expanded from small devices to large-scale devices, such as electric vehicles and smart grids.[3] However, the large-scale energy device application of LIBs was hindered by safety issues of LIBs, limited lithium resources in the earth's crust and high cost.[4,5] Thus, non-lithium-ion batteries (NLIBs) were considered as the next generation of renewable energy technologies, for instance, batteries of Na ion,[6,7] K ion,[8,9] Ca ion,[10,11] Mg ion,[12–15] Al ion,[16,17] and Zn ion[18,19] due to their abundant natural resources, suitable negative redox potentials and operational safety.[20,21]

It should be noted that whether it was a LIB or an NLIB, the properties of the electrode materials with excellent cycling stability, satisfactory rate capability, and high specific capacity were the key to determining battery performance.[21,22] However, compared with the in-depth study of cathode materials such as open framework materials,[23,24] layered transition-metal oxides,[25,26] and polyanionic compounds,[22,27] the research progress of anode materials was much slower. Composite materials of group IVA, VA element-based metal alloys and carbon-based materials have been shown to be applicable for LIBs.[28–30] Although carbon-based materials have been greatly improved in terms of safety and cycling performance, these materials were not ideal anode materials for NLIBs. Thus, it is critical to find suitable anode materials with high capacity and fast ion insertion/extraction for NLIBs.

'MXenes' are a class of two-dimensional (2D) transition-metal carbide materials, and are exfoliated from the MAX phase (M = Ti, Sr, V, Cr, Ta, Nb, Zr, Mo, or Hf, A = IIIA or IVA, and X = C and/or N).[31–33] MXenes are considered as the ideal anode materials for NLIBs owing to their remarkable mechanical properties, high specific surface area, and unique structure enabling fast ion insertion/extraction.[34,35] Moreover, when MXenes are used as the anode materials of electrodes, Li^+, Na^+, K^+, Mg^{2+}, Ca^{2+}, and Al^{3+} could be intercalated into MXenes.[35–37]

Recently, we designed a novel tetragonal TiC (tetr-TiC) by using the first-principles calculations.[38] State-of-the-art calculations showed that tetr-TiC had high thermal stability, excellent lithium-ion storage, and a low potential diffusion barrier.[38] Besides, we demonstrated that several other former transition metal carbides were dynamically stable, including tetr-ScC, tetr-CrC, tetr-VC, tetr-ZrC, tetr-NbC, tetr-TaC, and tetr-HfC. From the phonon spectrum calculation results, it could be observed that the Brillouin zone frequencies of tetr-MCs were positive, which

College of Materials Science and Engineering, Zhejiang University of Technology, Hangzhou 310014, China. E-mail: huxj@zjut.edu.cn

† Electronic supplementary information (ESI) available. See DOI: 10.1039/d0cp00839g

‡ These authors contributed equally to this work.

proved that tetr-MCs were dynamically stable.[38] This suggests that if the ions of Na^+, K^+, Mg^{2+}, Ca^{2+}, and Al^{3+} can be intercalated into these novel tetr-MCs, there is a chance to discover new potential anode materials. Therefore, our research objective is to systematically investigate the stability and performance of Na^+, K^+, Mg^{2+}, Ca^{2+}, Zn^{2+}, and Al^{3+} on tetr-MCs and to find appropriate anode materials for NLIBs.

In this work, we performed a computational investigation on the electronic properties of tetr-MCs, a new class of 2D materials proposed by us recently.[38] All proposed tetr-MCs exhibit intrinsic metallic conductivity, indicating their potential application in NLIBs as their analogue MXene materials. Moreover, we systematically studied the adsorption, storage capacity, and diffusion energy barriers of metal ions (Na^+, K^+, Mg^{2+}, Ca^{2+}, Zn^{2+}, and Al^{3+}) on the tetr-MC surfaces to explore their application as anode materials for NLIBs. tetr-VC and tetr-TiC monolayers, because of their combined remarkable properties, including intrinsic metallic conductivity, high theoretical capacity, low ion diffusion barrier, and low average open circuit voltage (OCV), have great potential as alternative anode materials to MXenes for NLIBs. The current results provide important guidance for experimentalists to search suitable anode materials for NLIBs with excellent performance.

2. Methods

All structural relaxation, total energy, and electronic structure calculations were carried out using the generalized gradient approximation (GGA) of the Perdew–Burke–Ernzerhof (PBE) exchange correlation functional, as implemented in the Vienna Ab initio Simulation Package (VASP, version 5.4.4)[39] for carrying out the projector-augmented wave (PAW) method.[40] The cut-off energy was set to be 650 eV, and the Monkhorst–Pack k meshes of $8 \times 8 \times 1$ were used to give a sufficient convergence of the total energies during the structural relaxation.[41] Moreover, we used PBE exchange–correlation potential to calculate the density of states (DOS) with a denser k grid of $24 \times 24 \times 1$, after structures reaching the required accuracy. It should be noted that the band gaps will be well underestimated by using the PBE functional, so we utilized the Heyd–Scuseria–Ernzerhof (HSE06) functional to calculate the corrected band structure.[38] Meanwhile, the long-range interactions in the metal atom adsorbed systems were also included by using the density functional theory (DFT)-D2 method of the Grimme van der Waals (vdW) correction.[42] We ensured that the vacuum space was at least 15 Å in all calculations, in order to prevent artificial interlayer interactions caused by periodic boundary conditions. The in-plane stiffness and Poisson's ratio can be derived from the elastic constants using the following equation

$$E_a = \frac{C_{11}C_{22} - C_{12}C_{21}}{C_{22}}, \quad E_b = \frac{C_{11}C_{22} - C_{12}C_{21}}{C_{11}} \tag{1}$$

$$V_a = \frac{C_{21}}{C_{22}}, \quad V_b = \frac{C_{12}}{C_{11}} \tag{2}$$

where E_a and E_b are the in-plane stiffness, V_a and V_b are Poisson's ratio. And we also considered the vdW interactions to research the metal atom adsorption and diffusion energy barriers on tetr-MCs. The climbing-image nudged elastic band (CI-NEB) method[43] was used to calculate the diffusion energy barrier and minimum energy path of the metal atoms on the tetr-MC structures. The initial guess of the diffusion barrier pathway has been generated by linear interpolation using 6 images between the initial and final points of the diffusion energy barrier path. The geometry and energy of the images were optimized until the total energies became $<10^{-4}$ eV with a cutoff energy of 650 eV. In order to measure the stability of the adsorption of the isolated metal atoms on the surface of tetr-MCs, the following equations were used to calculate the adsorption energy:

$$E_{ad} = E_{total} - E_M - E_{tetr\text{-}MCs} \tag{3}$$

where E_{total}, E_M, and $E_{tetr\text{-}MCs}$ are the total energies of metal-adsorbed tetr-MCs, a metal atom (in the bulk phase), and tetr-MCs, respectively. The charging and discharging processes of the tetr-MC anode could be assumed to follow the chemical eqution shown below:

$$MC + xA^{n+} + xne^- \leftrightarrow MC - A_x \tag{4}$$

Therefore, the OCV could be estimated using the following equation (volume and entropy effects are neglected):[44,45]

$$OCV \approx \frac{E_{tetr\text{-}MC} + xE_A - E_{tetr\text{-}MC\text{-}A_x}}{x} \tag{5}$$

where $E_{tetr\text{-}MC}$, $E_{tetr\text{-}MC\text{-}A_x}$, and E_A are the potential energies of tetr-MC, tetr-MC-A_x, and metal, respectively (M = Sc, Ti, V, Cr, Zr, Nb, Hf, and Ta, A = K, Na, Ca, Mg, Al, and Zn).

3. Results and discussion

3.1 Structural and electronic properties

Fig. 1a presents the structure of the tetr-MCs in a tetragonal lattice, in which the blue color balls represent early transition metal atoms and the brown color balls represent carbon atoms. The optimized lattice parameters of a, b and c are in the range of 1.97 Å to 3.27 Å. The calculated structural parameters and atomic positions of tetr-MCs are listed in Table S1 (ESI†). The bond angle between the metal atom and two carbon atoms is about 93 degree, which is close to vertical, as can also be seen from Fig. 1a. It should be noted that tetr-MCs have a perfect flat structure instead of a buckling structure. Besides, each metal atom is bonded to five C atoms, suggesting that the metal atoms on the surface are bare, which will undoubtedly affect the stability of tetr-MCs. In our previous work, we have carried out phonon spectra simulations to prove that these eight structures are kinetically stable.[38] Moreover, we calculated the elastic constants, in-plane stiffness (the analogue of Young's modulus for 2D materials) and Poisson's ratio of tetr-MCs to explore if tetr-MCs are strong enough to resist mechanical deformations. Usually, the elastic constants need to meet the conditions of $C_{11}C_{22} - C_{12}C_{21} > 0$ and $C_{66} > 0$ for a mechanically stable 2D structure.[41,46] The elastic constant values only need to be satisfied with $C_{11} > |C_{12}|$ and $C_{66} > 0$ as a result of the tetragonal

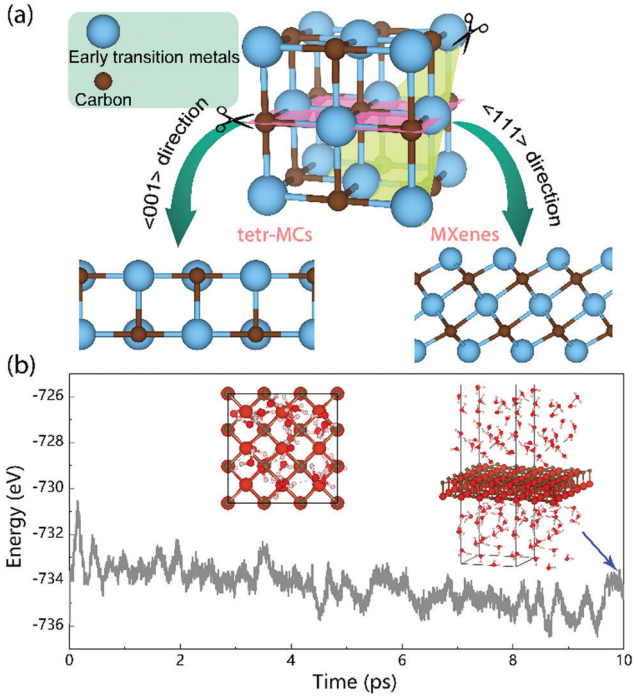

Fig. 1 (a) The design scheme of novel tetr-MCs. From structural connectivity, the MXenes can be viewed as the bulk phase of transition metal carbide cutting along the ⟨111⟩ direction, while cutting along the ⟨001⟩ direction the tetr-MC structure can be viewed. The blue and brown spheres represent the early transition metals (Sc, Cr, V, Zr, Ti, Nb, Ta, and Hf) and carbon atoms, respectively. (b) The fluctuations of total energy of tetr-VC with a lot of water molecules arranged in a 3 × 3 supercell as a function of the *ab initio* molecular dynamics (AIMD) step at 300 K (up to 10 ps). The insets are a top view (left) of tetr-VC with a lot of water molecules and a side view (right) after 10 ps simulation. The trajectories of the structures are stable over the entire length of simulation time at 300 K.

symmetry of tetr-MCs. As shown in Table S2 (ESI†), the elastic constants of tetr-MCs are in agreement with the mechanical stability criterion for 2D sheets, indicating that the structures are strong enough to resist mechanical deformations without the support of a specific substrate. It is worth noting that the in-plane stiffness of tetr-ScC is only 137.2 GPa nm, which is lower than those of other tetr-MC materials. Because the radius of the Sc atom is larger than those of other atoms, the structure of tetr-ScC is not stable compared with other structures.

Besides, we calculated the volume expansion (*i.e.* change in lattice parameters), in-plane stiffness and Poisson's ratio of tetr-VC with increased concentrations of Mg ions in order to evaluate its mechanical properties. Generally, an axial compression is applied to cause an expansion in the transverse direction. It is observed that from Tables S1–S3 (ESI†), as the concentrations of Mg ions increase, the lattice constants a and b of tetr-VC-Mg_x increase from 2.864 Å to 2.924 Å, while c becomes smaller, ranging from 1.995 Å to 2.040 Å. Furthermore, the in-plane stiffness of tetr-VC-Mg_x increases from 215.1 GPa nm to 350.8 GPa nm with x increasing from 0 to 2, which means that the material becomes less susceptible to deformation and has stronger ability to resist elastic deformation. In addition, the Poisson's ratio of tetr-VC-Mg_x decreases from 0.40 to 0.15 as x increases, indicating that the material is in the elastic working range.

Next, we systematically studied the electronic properties of tetr-MCs and their application advantages in NLIBs. Firstly, we calculated the band structure by using the PBE functional. As shown in Fig. S1 (ESI†), the electronic band structures at the Fermi energy demonstrate the metallic properties of all tetr-MCs, which ensure the good electronic conductivity of the tetr-MCs. We also investigated the electronic properties of these configurations by using the hybrid HSE06 functional, due to the well-known significant underestimation of the band gaps of the conventional GGA/PBE calculations, as shown in Fig. S2 (ESI†). It is observed that the tetr-MCs still show metallic properties. To explain the origin of the metallicity of tetr-MCs, we performed a projected DOS analysis of atomic orbitals of metal and C atoms, as shown in Fig. S3–S5 (ESI†). It is found that the energy bands near the Fermi level are mainly contributed by the d orbital of the metal atom, while the M_{3s} or M_{4s} or M_{5s}, C_{2s}, and C_{2p} give only a small contribution to the metallicity of tetr-MCs. Unusually, the energy band near the Fermi level of tetr-ScC is also contributed by the 2p orbital of the C atom.

It is very important to show whether the tetr-MCs are stable under more realistic conditions than in a vacuum. Considering that the diffusion barriers of Mg and Al on tetr-VC are relatively low, we performed AIMD simulations to calculate the structure of tetr-VC with a lot of water molecules arranged in a 3 × 3 supercell in order to prove the stability of the tetr-MCs. The inset of Fig. 1b shows the schematic diagram of the structure of tetr-VC with a large number of water molecules after the optimization of the structure, and the other one is a top view of tetr-VC with a lot of water molecules. It is observed that there is no structural reconstruction found in the simulation processes at 300 K for 10 ps with a time step of 1 fs, as shown in Fig. 1b, indicating that tetr-MCs are expected to be highly stable in more realistic environments.

3.2 Metal ion storage on the tetr-MC surface

It is well accepted that the performance of anode materials in NLIBs is largely dependent on the diffusion rate of metal atoms on the anode surface. Therefore, we inspected the metal atom adsorption and diffusion behaviors on the tetr-MCs. We firstly consider the optimal adsorption sites for the Mg atom on tetr-MCs with a 2 × 2 unit cell because the redox potential and diffusion energy barrier of tetr-MCs are affected by the atomic position of the intercalated atoms. As shown in Fig. S6 (ESI†), we selected three positions on tetr-MCs to place the Mg atom on the C site, hole site, and metal site, respectively, and calculate their adsorption energies. Table S4 (ESI†) lists that the Mg atom has the lowest adsorption energy at the C position, indicating that it is the best adsorption site at the C position on tetr-MCs except tetr-CrC and tetr-ScC and the best adsorption site of Mg on tetr-CrC and tetr-ScC is the hole position for its lowest adsorption energy at the hole site. Thus, for a tetr-MC unit cell, we calculated the adsorption energies of tetr-MCs with two, three, and four absorbed metal atoms, like K, Na, Mg, Ca, Zn, and Al, respectively, showing MC-A_x (M is an early transition

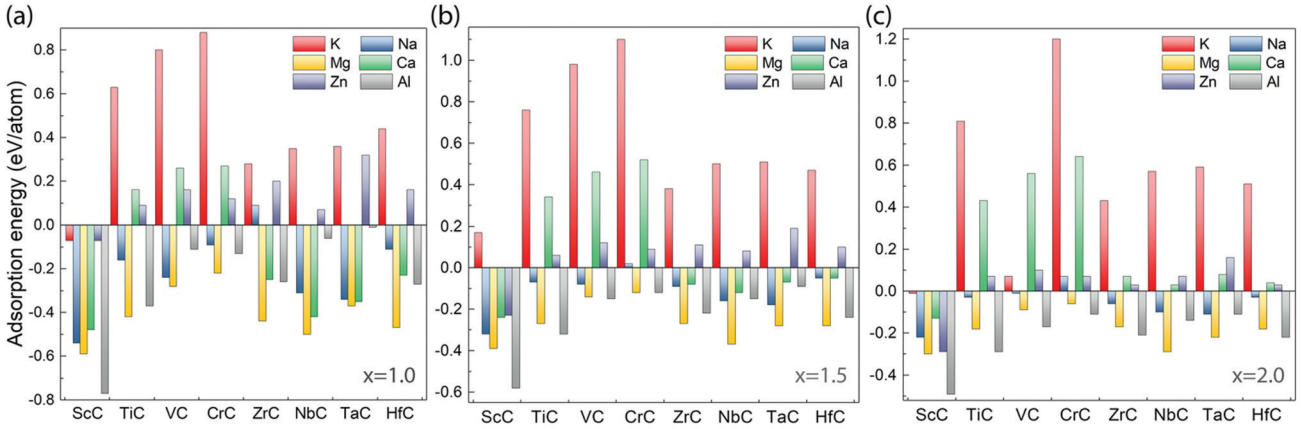

Fig. 2 The adsorbed energy of (a) tetr-MC-$A_{x=1}$, (b) tetr-MC-$A_{x=1.5}$ and (c) tetr-MC-$A_{x=2}$.

metal and A is the adsorbed metal atom) stoichiometry. And we calculated the corresponding adsorption energy for the adsorption site (on top of the C atom for tetr-TiC, tetr-VC, tetr-ZrC, tetr-NbC, tetr-TaC and tetr-HfC, and on the hole for tetr-ScC and tetr-CrC). The calculated adsorption energies using the DFT-D2 corrected functional are summarized in Fig. 2.

Fig. 2a shows when $x = 1$, most of the adsorption energies are negative, like for Na, Mg and Al, suggesting that these atoms are well adsorbed by tetr-MCs. In addition to tetr-ScC, the adsorption energies of K and Zn on tetr-MCs are positive, which means that they are either physisorbed or partially chemisorbed. The adsorption energy of K is much larger than those of other atoms, even reaches 0.88 eV on tetr-CrC. This may relate to the strong Coulomb repulsion between K and the M atoms due to the excessive atomic radius of K. Ca should show a similar behaviour due to its large atomic radius, however, the adsorption energies of Ca on tetr-MCs are partially positive. This may be induced by the larger distance between Ca and metal atoms, which reduces the Coulomb interaction.

Fig. 2b and c show that as the concentration of K increases, the adsorption energies of K on tetr-MCs are almost positive (up to 1.2 eV). It is difficult for K to be adsorbed on tetr-MCs. Contrary to K, the adsorption energies of Na, Mg and Al on tetr-MCs are almost negative, revealing that they can form a full adsorption layer on tetr-MCs. Ca and Zn have moderate positive adsorption energies (0–0.6 eV) on tetr-MCs, indicating that they may form partial layers.

As mentioned above, the adsorption energies of K and Zn on tetr-MCs are almost positive, suggesting that they are either physisorbed or partially chemisorbed. With increasing K and Zn concentration, we found that adsorption energy of K is basically increasing, whereas that of Zn is almost decreasing. We explain this difference as follows: K is hardly absorbed by tetr-MCs because of the large atomic radius, and the Zn atom can donate more electrons than the K atom, thus the increased repulsion on adding further Zn atoms causes the instability for a full Zn adsorption layer.[21] The adsorption energies of Al, Mg, and Na are almost negative, and it means these atoms are well adsorbed by tetr-MCs. Furthermore, when $x < 2$, only on the tetr-TiC, tetr-VC, and tetr-CrC, the adsorption energy of Ca is positive. When $x = 2$, except for tetr-ScC, adsorption energy is negative, suggesting that with the Ca atom concentration further increases, the adsorption of Ca atoms continuously weakens because of the enhanced Ca–Ca repulsion. This trend is consistent with the trend of Li atoms reported in our previous work.[38]

3.3 Metal ion storage capacity and average OCV

In Fig. 3a–c, we show the theoretical capacities of tetr-MXA, tetr-MX-$A_{x=1.5}$, and tetr-MX-$A_{x=2}$ stoichiometry, respectively. When $x = 1$, tetr-ScC shows the highest capacity at 279, 335, 660, 552, 438, and 958 mA h g^{-1} for K, Na, Mg, Ca, Zn, and Al, respectively. These values are higher than the theoretical capacities of K, Na, Mg, Ca, and Al on Ti_2CO_2, and are comparable with the theoretical capacity of Ti_2C.[21] Besides, the capacity of Zn is slightly lower than the predicted high capacity of defective graphene.[10] It is found that the capacities of these metal atoms on tetr-TiC are larger in comparison to other 2D anode materials, such as graphite (284 mA h g^{-1} for Na[47]), phosphorene (315.52 mA h g^{-1} for Na and 310.71 mA h g^{-1} for Mg),[48] and MXenes (191.8 mA h g^{-1} for K, and 319.8 mA h g^{-1} for Ca).[37] Obviously, Mg and Al have larger theoretical capacities than those of other metal atoms on tetr-MCs, because compared with the monovalent ions, the multivalent metal ions can carry additional charges. In addition, even metal ions with the same valence state have different capacities on tetr-MCs due to their different atomic weights, for instance, K and Na. The heavier ions have lower theoretical capacities. Although the theoretical capacities increase as the concentration of metal atoms increases, the increase becomes smaller with each additional layer due to the increased weight.[21] It should be noted that the theoretical capacity of Al at a high concentration ($x = 2$) on tetr-ScC (up to 1450 mA h g^{-1}) is almost four times larger than that of the commercial graphite anode material.[28,49]

Compared with other metal ions, the theoretical capacities of Al on tetr-MCs are the highest, followed by Mg. In addition, Mg will not form dendrites,[50] which may puncture the separator material and cause a short circuit in the batteries. The absence of dendrites on the Al surface is considered to be a major

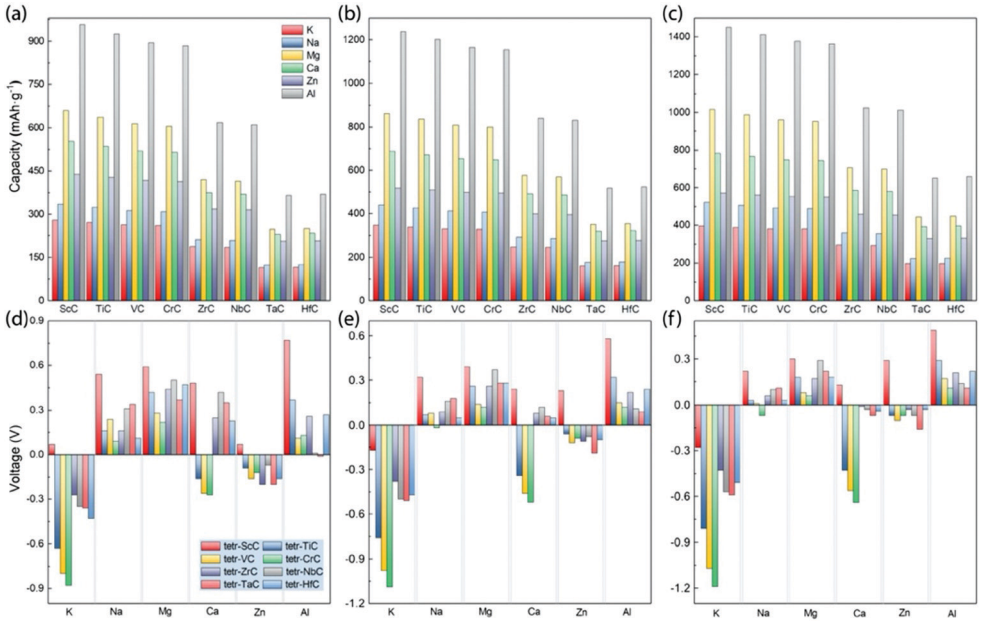

Fig. 3 The theoretical capacities of (a) tetr-MC-$A_{x=1}$, (b) tetr-MC-$A_{x=1.5}$ and (c) tetr-MC-$A_{x=2}$ and the average OCV of (d) tetr-MC-$A_{x=1}$, (e) tetr-MC-$A_{x=1.5}$ and (f) tetr-MC-$A_{x=2}$.

advantage of aluminum ion batteries.[51,52] Thus, stable multi-layer adsorption allows Mg and Al to have very high capacities on tetr-MCs if a reasonable electrolyte is used and the overall reaction rate is fast.

We then evaluated the average OCV of the tetr-MC-A_x, as shown in Fig. 3d–f, respectively. When x = 1, the average OCV values of K and Zn on tetr-MCs are negative except on tetr-ScC, indicating that the tetr-MCs might not be suitable anode materials for K-ion and Zn-ion batteries. Interestingly, this is in good agreement with the results of the adsorption energy. And the average OCV values of Na, Mg, and Al are in a good range, suggesting that the intercalation between Na, Mg, Al, and tetr-MCs is favorable. Moreover, the average OCV of Ca on tetr-MCs is partially positive. When x = 1.5 and x = 2, the situation is basically consistent with the results of the adsorption energy.

It is noted that the average OCV should be between 0.1–1.0 V for an anode material.[53] It is clear that the average OCV values of Na, Mg, and Al are almost in the range of 0.1–1.0 V, and those of K and Zn are almost negative, as the metal atom concentration is increased from x = 1 to x = 2. This reveals that the average OCV values of Na, Mg, and Al atoms on tetr-MCs are reasonable. Therefore, these OCV values indicate significant feasibility for tetr-MCs to be applied for Na-ion, Mg-ion and Al-ion batteries. And the tetr-MCs are promising as high-performance anode materials for NLIBs because of their reasonable OCV, higher theoretical storage capacity, and advanced electronic conductivity.

3.4 Metal ion diffusion on tetr-MCs

For anode electrode materials to exhibit great performance, they should not only have a high capacity and reasonable OCV, but also have a good charging/discharging rate. Then we combined storage capacity and OCV calculations to start calculating the metal atom migration on the tetr-MC surface, of Mg and Al, because of their outstanding capacities. In our previous work, two possible diffusion energy paths of a single metal atom on tetr-TiC were considered and the results showed that the barrier of the metal atom passing through a straight diffusion path was lower.[38] Thus, we only considered the straight diffusion path in this work. The CI-NEB method[43] was used to calculate the diffusion energy barriers of Mg and Al atoms on the tetr-MCs. The diffusion energy path of Mg and Al on a single layer of tetr-MCs except for tetr-ScC and tetr-CrC is as shown in Fig. 4.

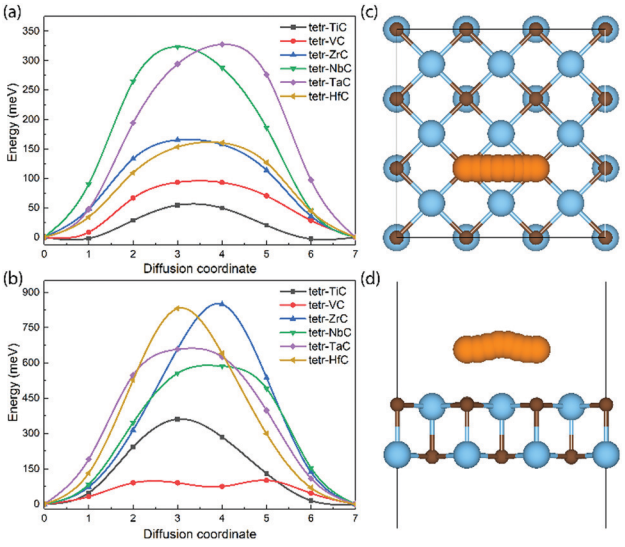

Fig. 4 The diffusion energy barrier of (a) Mg and (b) Al on tetr-TiC, tetr-VC, tetr-ZrC, tetr-NbC, tetr-TaC and tetr-HfC monolayers. (c) Top and (d) side views of the diffusion energy path with Mg and Al on tetr-TiC, tetr-VC, tetr-ZrC, tetr-NbC, tetr-TaC and tetr-HfC.

It is observed that the diffusion energy barriers of Mg on tetr-TaC and tetr-NbC are higher than those of Mg on other tetr-MCs, reaching 327 meV and 323 meV, respectively. Besides, the diffusion energy barrier of Mg on tetr-TiC is only 54 meV, which is much lower than those of Mg on previously proposed commercialized graphite anode materials (~400 meV) and TiO_2 (350–650 meV).[38] We speculate that there are two reasons for the low diffusion energy barrier of Mg on tetr-TiC. One is the surface appearance. For example, H. R. Jiang *et al.*[54] found that lithium atoms were more likely to diffuse along the furrow on the surface of borophene, and it was relatively difficult for them to migrate to neighboring furrows. Compared with MXenes, tetr-TiC has a smoother surface morphology, so it is easier for metal atoms to migrate on tetr-TiC. Another reason is the electronic properties. Mg transferred 0.76 *e* to O atoms on the Ti_2CO_2 surfaces.[21] From Bader charge analysis, we found that Mg transfers 0.48 *e* to tetr-TiC, and about 0.33 *e* are transferred to the C atom directly below Mg. This shows that Mg is more ionized on MXenes than on tetr-TiC, as a result, Mg has a low diffusion barrier on tetr-TiC. It can be clearly seen from Fig. S7 (ESI†) that there is electron accumulation around the tetr-TiC, whereas electron depletion appears around the Mg atom. These results also indicate that electrons are transferred from the Mg atom to tetr-TiC. In other words, the adsorbed Mg atom behaves as an electron donor. Therefore, the Mg atom on the tetr-TiC can provide a higher reaction rate than on other tetr-MCs and 2D materials. Surprisingly, the diffusion energy barriers of Mg on tetr-ScC and tetr-CrC are negative, which means that the optimal adsorption position of Mg on tetr-ScC and tetr-CrC may be in the middle of two C atoms rather than directly above the C atoms. Thus, we recalculated the diffusion barriers of Mg on tetr-ScC and tetr-CrC, and selected the lowest energy of the previous step as a new starting point. Besides, we selected two different paths to calculate the diffusion energy barriers of Mg on tetr-ScC and tetr-CrC, as shown in Fig. 5a, c and d, respectively.

The diffusion barriers of Al on tetr-HfC and ZrC are higher than 800 meV, but the diffusion barrier on tetr-VC is only 101 meV. Similarly, the diffusion energy barriers of Al on tetr-ScC and tetr-CrC are negative, and then we recalculated the diffusion barriers of Al on tetr-ScC and tetr-CrC, the diffusion energy barriers and top view of two paths for Al on tetr-ScC and tetr-CrC are shown in Fig. 5b–d, respectively. Fig. 5a and c show that the values of the migration barrier energy calculated using the two different migration paths are very close, and the diffusion barriers of Mg on tetr-ScC and tetr-CrC are smaller than those of Al. Surprisingly, the Mg or Al atom will move to the vicinity of the C atom firstly and then to another vacancy center, instead of moving directly from one vacancy center to another one because the C atom is connected to four large metal atoms on the surface of the tetr-MCs. When the Mg or Al atom migrates from one vacancy to another, it is easier to move closer to the C atom rather than to the metal atoms due to the large volume of the base metal atoms.

As shown in Fig. 6a–c, the evolution of total energy of Mg and Al on tetr-VC at 300 K demonstrates that no structural

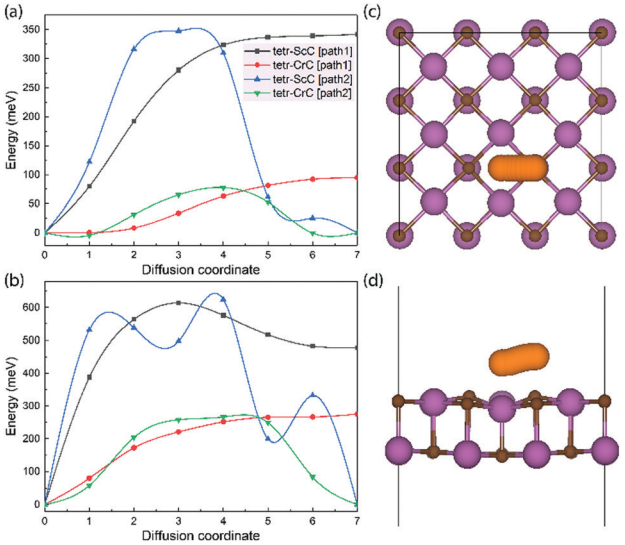

Fig. 5 The diffusion energy barriers of (a) Mg and (b) Al on tetr-ScC and tetr-CrC and the top view of the diffusion energy (c) path1 and (d) path2 with Mg and Al on tetr-ScC and tetr-CrC, respectively.

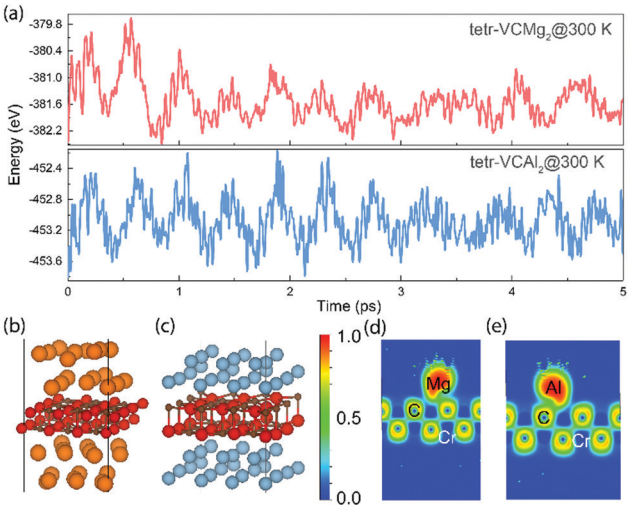

Fig. 6 (a) The fluctuations of total energy of Mg and Al on the tetr-VC 3 × 3 supercell as a function of the AIMD step at 300 K. The trajectories of the structures are stable over the entire length of simulation time at 300 K. (b) Mg and (c) Al of the equilibrium structures at a temperature of 300 K, at the end of 5 ps AIMD simulations. The electron localization function (ELF) maps of (d) a single Mg atom on tetr-CrC and (e) a single Al atom on tetr-CrC.

reconstruction is found in all of the simulation processes after heating at 300 K for 5 ps with a time step of 1 fs. Meanwhile, we separately calculated the electron localization function (ELF) of a single, one layer, two layers of Mg and Al on tetr-NbC and tetr-CrC. As seen in Fig. 6d, e and Fig. S8, S9 (ESI†), it is similar to the electronic structures for adsorbed Mg and Al on tetr-MCs, and the electron delocalization is in line with the excellent electric conductivity.

As mentioned above, the tetr-MCs exhibit a larger diffusion energy barrier for Al than that for Mg, because of the stronger interaction between the Al and tetr-MCs. Thus, Al^{3+} diffusion in

the structures is harder than Mg^{2+} diffusion. Other than this, we found that the lowest energy sites of Mg and Al atoms on tetr-ScC and tetr-CrC are in the hole between the two C atoms, while Mg and Al atoms are directly above the C atom on the remaining tetr-MCs. The results show that the diffusion energy barriers of Mg and Al on tetr-ScC are greater than those on tetr-CrC. Meanwhile, the migration barriers of the Mg atom on tetr-TiC and tetr-VC are 54 meV and 93 meV, while those of the Al atom on tetr-TiC and tetr-VC are 360 meV and 101 meV. It is clear that the Mg atom has a better migration rate on tetr-MCs than Al. Mg and Al on tetr-ScC may possess high capacities, while the rate performances of Mg and Al on tetr-ScC will not be as good as those of Mg and Al on tetr-VC, tetr-TiC and tetr-CrC.

In order to further explore the situation of the multiple atom diffusion barrier, we selected two Mg atoms on tetr-VC to perform NEB calculations. As shown in Fig. S10 (ESI†), it can be seen that the diffusion barrier of double Mg atoms on tetr-VC is only 65 meV, which is lower than that for the single Mg atom migration. Due to the Coulomb interaction force between two Mg atoms, they move almost parallel and do not reunite. It might be the concerted migration for fast diffusion in multiple Mg atoms on tetr-VC, which means high-energy sites are occupied along the diffusion path by the mobile Mg atom, thereby activating migration and reducing the diffusion energy barrier.[55]

4. Conclusions

In summary, we have systematically investigated the tetr-MCs as potential anode materials for NLIBs using first-principles computation. We found that there are two cases of the optimal adsorption position of metal atoms on tetr-MCs. One is that the metal atom will be in the hole site on tetr-ScC and tetr-CrC, and on the other tetr-MCs it will be above the C atom. Our results show that tetr-MCs are promising anode materials with excellent electrical conductivity, a suitable open circuit voltage (0.05–0.77 V), and a high storage capacity (up to 1450 mA h g^{-1}) for NLIBs, for Mg and Al ion batteries in particular. The results reveal that diffusion barriers for the Mg atom on tetr-TiC and those for the Al atom on tetr-VC are not higher than 101 meV, indicating the high-speed ion charge/discharge rate. Furthermore, Ca^{2+} and Zn^{2+} are structurally stable on some tetr-MCs, and the storage capacities are relatively high. Unfortunately, monovalent ions, for instance, K^+ and Na^+ have low storage capacities on tetr-MCs and even as the ion concentration increases, the tendency for storage capacity to increase is not large. Our results provide insight into metal ion storage capacity on novel 2D tetr-MCs and suggest a route to prepare high performance ion batteries by using non-monovalent cations.

Author contributions

X. Hu, C. Ke, and D. Fan designed the research. C. Ke and D. Fan carried out the *ab initio* calculations and interpreted the data. C. Ke wrote the manuscript with the support from D. Fan, C. Chen, X. Li, and M. Jiang. X. Hu coordinated the research.

Conflicts of interest

There are no conflicts to declare.

Acknowledgements

This work was performed at the National Supercomputer Center in Guangzhou, and the calculations were carried out on TianHe-2. This work was supported by the Key Project of the National Natural Science Foundation of China (U1809210), National Key Research and Development Program of China under Grant No. 2016YFE0133200, and the National Natural Science Foundation of China (Grant No. 11504325, 50972129, and 50602039). This work was also supported by the International Science Technology Cooperation Program of China (2014DFR51160), the European Union's Horizon 2020 Research and Innovation Staff Exchange (RISE) Scheme (No. 734578), Natural Science Foundation of Zhejiang Province (LQ15A040004), and the One Belt and One Road International Cooperation Project from the Key Research and Development Program of Zhejiang Province (No. 2018C04021).

Notes and references

1 D. P. Dubal, O. Ayyad, V. Ruiz and P. Gómez-Romero, Hybrid energy storage: the merging of battery and supercapacitor chemistries, *Chem. Soc. Rev.*, 2015, **44**, 1777–1790.
2 W. Li, B. Song and A. Manthiram, High-voltage positive electrode materials for lithium-ion batteries, *Chem. Soc. Rev.*, 2017, **46**, 3006–3059.
3 Y. Zhao, Y. Ding, Y. Li, L. Peng, H. R. Byon, J. B. Goodenough and G. Yu, A chemistry and material perspective on lithium redox flow batteries towards high-density electrical energy storage, *Chem. Soc. Rev.*, 2015, **44**, 7968–7996.
4 J. B. Goodenough and K. S. Park, The Li-Ion Rechargeable Battery: A Perspective, *J. Am. Chem. Soc.*, 2013, **135**, 1167–1176.
5 J. M. Tarascon, Is lithium the new gold?, *Nat. Chem.*, 2010, **2**, 510.
6 J. S. Park and Y. C. Kang, Uniquely structured Sb nanoparticle-embedded carbon/reduced graphene oxide composite shell with empty voids for high performance sodium-ion storage, *Chem. Eng. J.*, 2019, **373**, 227–237.
7 M. D. Slater, D. Kim, E. Lee and C. S. Johnson, Sodium-Ion Batteries, *Adv. Funct. Mater.*, 2013, **23**, 947–958.
8 C. D. Wessells, S. V. Peddada, R. A. Huggins and Y. Cui, Nickel Hexacyanoferrate Nanoparticle Electrodes For Aqueous Sodium and Potassium Ion Batteries, *Nano Lett.*, 2011, **11**, 5421–5425.
9 M. Tao, G. Du, Y. Zhang, W. Gao, D. Liu, Y. Luo, J. Jiang, S. Bao and M. Xu, TiO_xN_y nanoparticles/C composites derived from MXene as anode material for potassium-ion batteries, *Chem. Eng. J.*, 2019, **369**, 828–833.
10 D. Datta, J. Li and V. B. Shenoy, Defective Graphene as a High-Capacity Anode Material for Na- and Ca-Ion Batteries, *ACS Appl. Mater. Interfaces*, 2014, **6**, 1788–1795.

11 R. Y. Wang, C. D. Wessells, R. A. Huggins and Y. Cui, Highly Reversible Open Framework Nanoscale Electrodes for Divalent Ion Batteries, *Nano Lett.*, 2013, **13**, 5748–5752.
12 T. S. Arthur, N. Singh and M. Matsui, Electrodeposited Bi, Sb and $Bi_{1-x}Sb_x$ alloys as anodes for Mg-ion batteries, *Electrochem. Commun.*, 2012, **16**, 103–106.
13 H. D. Yoo, I. Shterenberg, Y. Gofer, G. Gershinsky, N. Pour and D. Aurbach, Mg rechargeable batteries: an on-going challenge, *Energy Environ. Sci.*, 2013, **6**, 2265.
14 N. Amir, Y. Vestfrid, O. Chusid, Y. Gofer and D. Aurbach, Progress in nonaqueous magnesium electrochemistry, *J. Power Sources*, 2007, **174**, 1234–1240.
15 K. W. Nam, S. Kim, S. Lee, M. Salama, I. Shterenberg, Y. Gofer, J. S. Kim, E. Yang, C. S. Park, J. S. Kim, S. S. Lee, W. S. Chang, S. G. Doo, Y. N. Jo, Y. Jung, D. Aurbach and J. W. Choi, The High Performance of Crystal Water Containing Manganese Birnessite Cathodes for Magnesium Batteries, *Nano Lett.*, 2015, **15**, 4071–4079.
16 N. Jayaprakash, S. K. Das and L. A. Archer, The rechargeable aluminum-ion battery, *Chem. Commun.*, 2011, **47**, 12610.
17 D. Y. Wang, C. Y. Wei, M. C. Lin, C. J. Pan, H. L. Chou, H. A. Chen, M. Gong, Y. Wu, C. Yuan, M. Angell, Y. J. Hsieh, Y. H. Chen, C. Y. Wen, C. W. Chen, B. J. Hwang, C. C. Chen and H. Dai, Advanced rechargeable aluminium ion battery with a high-quality natural graphite cathode, *Nat. Commun.*, 2017, **8**, 14283.
18 F. Liu, Z. Chen, G. Fang, Z. Wang, Y. Cai, B. Tang, J. Zhou and S. Liang, V2O5 Nanospheres with Mixed Vanadium Valences as High Electrochemically Active Aqueous Zinc-Ion Battery Cathode, *Nano-Micro Lett.*, 2019, **11**, 25.
19 J. Wang, J. G. Wang, H. Liu, C. Wei and F. Kang, Zinc ion stabilized MnO_2 nanospheres for high capacity and long lifespan aqueous zinc-ion batteries, *J. Mater. Chem. A*, 2019, **7**, 13727–13735.
20 P. Xiang, X. Chen, W. Zhang, J. Li, B. Xiao, L. Li and K. Deng, Metallic borophene polytypes as lightweight anode materials for non-lithium-ion batteries, *Phys. Chem. Chem. Phys.*, 2017, **19**, 24945–24954.
21 Y. Xie, Y. Dall'Agnese, M. Naguib, Y. Gogotsi, M. W. Barsoum, H. L. Zhuang and P. R. C. Kent, Prediction and Characterization of MXene Nanosheet Anodes for Non-Lithium-Ion Batteries, *ACS Nano*, 2014, **8**, 9606–9615.
22 S. W. Kim, D. H. Seo, X. Ma, G. Ceder and K. Kang, Electrode Materials for Rechargeable Sodium-Ion Batteries: Potential Alternatives to Current Lithium-Ion Batteries, *Adv. Energy Mater.*, 2012, **2**, 710–721.
23 X. Bie, K. Kubota, T. Hosaka, K. Chihara and S. Komaba, A novel K-ion battery: hexacyanoferrate(II)/graphite cell, *J. Mater. Chem. A*, 2017, **5**, 4325–4330.
24 Y. Lu, L. Wang, J. Cheng and J. B. Goodenough, Prussian blue: a new framework of electrode materials for sodium batteries, *Chem. Commun.*, 2012, **48**, 6544.
25 G. G. Amatucci, F. Badway, A. Singhal, B. Beaudoin, G. Skandan, T. Bowmer, I. Plitz, N. Pereira, T. Chapman and R. Jaworski, Investigation of Yttrium and Polyvalent Ion Intercalation into Nanocrystalline Vanadium Oxide, *J. Electrochem. Soc.*, 2001, **148**, A940.
26 X. Xiang, K. Zhang and J. Chen, Recent Advances and Prospects of Cathode Materials for Sodium-Ion Batteries, *Adv. Mater.*, 2015, **27**, 5343–5364.
27 G. A. Tritsaris, E. Kaxiras, S. Meng and E. Wang, Adsorption and Diffusion of Lithium on Layered Silicon for Li-Ion Storage, *Nano Lett.*, 2013, **13**, 2258–2263.
28 Y. Cao, L. Xiao, M. L. Sushko, W. Wang, B. Schwenzer, J. Xiao, Z. Nie, L. V. Saraf, Z. Yang and J. Liu, Sodium Ion Insertion in Hollow Carbon Nanowires for Battery Applications, *Nano Lett.*, 2012, **12**, 3783–3787.
29 Y. Zhu, X. Han, Y. Xu, Y. Liu, S. Zheng, K. Xu, L. Hu and C. Wang, Electrospun Sb/C Fibers for a Stable and Fast Sodium-Ion Battery Anode, *ACS Nano*, 2013, **7**, 6378–6386.
30 J. Qian, Y. Xiong, Y. Cao, X. Ai and H. Yang, Synergistic Na-Storage Reactions in Sn_4P_3 as a High-Capacity, Cycle-stable Anode of Na-Ion Batteries, *Nano Lett.*, 2014, **14**, 1865–1869.
31 Q. Tang, Z. Zhou and Z. Chen, Innovation and discovery of graphene-like materials via density-functional theory computations: Innovation and discovery of graphene-like materials via DFT computations, *WIREs Comput. Mol. Sci.*, 2015, **5**, 360–379.
32 M. Naguib, M. Kurtoglu, V. Presser, J. Lu, J. Niu, M. Heon, L. Hultman, Y. Gogotsi and M. W. Barsoum, Two-Dimensional Nanocrystals Produced by Exfoliation of Ti_3AlC_2, *Adv. Mater.*, 2011, **23**, 4248–4253.
33 F. Chang, C. Li, J. Yang, H. Tang and M. Xue, Synthesis of a new graphene-like transition metal carbide by de-intercalating Ti_3AlC_2, *Mater. Lett.*, 2013, **109**, 295–298.
34 H. Zhang, Ultrathin Two-Dimensional Nanomaterials, *ACS Nano*, 2015, **9**, 9451–9469.
35 M. R. Lukatskaya, O. Mashtalir, C. E. Ren, Y. Dall'Agnese, P. Rozier, P. L. Taberna, M. Naguib, P. Simon, M. W. Barsoum and Y. Gogotsi, Cation Intercalation and High Volumetric Capacitance of Two-Dimensional Titanium Carbide, *Science*, 2013, **341**, 1502–1505.
36 Y. X. Yu, Prediction of Mobility, Enhanced Storage Capacity, and Volume Change during Sodiation on Interlayer-Expanded Functionalized Ti_3C_2 MXene Anode Materials for Sodium-Ion Batteries, *J. Phys. Chem. C*, 2016, **120**, 5288–5296.
37 D. Er, J. Li, M. Naguib, Y. Gogotsi and V. B. Shenoy, Ti_3C_2 MXene as a High Capacity Electrode Material for Metal (Li, Na, K, Ca) Ion Batteries, *ACS Appl. Mater. Interfaces*, 2014, **6**, 11173–11179.
38 D. Fan, S. Lu, Y. Guo and X. Hu, Two-Dimensional Tetragonal Titanium Carbide: a High-Capacity and High-Rate Battery Material, *J. Phys. Chem. C*, 2018, **122**, 15118–15124.
39 G. Kresse and J. Furthmüller, Efficient iterative schemes for *ab initio* total-energy calculations using a plane-wave basis set, *Phys. Rev. B: Condens. Matter Mater. Phys.*, 1996, **54**, 11169–11186.
40 J. P. Perdew, K. Burke and M. Ernzerhof, Generalized Gradient Approximation Made Simple, *Phys. Rev. Lett.*, 1996, **77**, 3865–3868.
41 D. Fan, S. Lu, Y. Guo and X. Hu, Two-dimensional stoichiometric boron carbides with unexpected chemical bonding and promising electronic properties, *J. Mater. Chem. C*, 2018, **6**, 1651–1658.

42 S. Grimme, Semiempirical GGA-type density functional constructed with a long-range dispersion correction, *J. Comput. Chem.*, 2006, **27**, 1787–1799.
43 G. Henkelman, B. P. Uberuaga and H. Jónsson, A climbing image nudged elastic band method for finding saddle points and minimum energy paths, *J. Chem. Phys.*, 2000, **113**, 9901–9904.
44 Q. Tang, Z. Zhou and P. Shen, Are MXenes Promising Anode Materials for Li Ion Batteries? Computational Studies on Electronic Properties and Li Storage Capability of Ti_3C_2 and $Ti_3C_2X_2$ (X = F, OH) Monolayer, *J. Am. Chem. Soc.*, 2012, **134**, 16909–16916.
45 D. Fan, A. A. Golov, A. A. Kabanov, C. Chen, S. Lu, X. Li, M. Jiang and X. Hu, A New sp^2–sp^3 -Hybridized Metallic Carbon Network for Lithium-Ion Battery Anode with Enhanced Safety and Lithium-Ion Diffusion Rate, *J. Phys. Chem. C*, 2019, **123**, 15412–15418.
46 S. Zhang, J. Zhou, Q. Wang, X. Chen, Y. Kawazoe and P. Jena, Penta-graphene: A new carbon allotrope, *Proc. Natl. Acad. Sci. U. S. A.*, 2015, **112**, 2372–2377.
47 Y. Wen, K. He, Y. Zhu, F. Han, Y. Xu, I. Matsuda, Y. Ishii, J. Cumings and C. Wang, Expanded graphite as superior anode for sodium-ion batteries, *Nat. Commun.*, 2014, **5**, 4033.
48 A. Sibari, A. Marjaoui, M. Lakhal, Z. Kerrami, A. Kara, M. Benaissa, A. Ennaoui, M. Hamedoun, A. Benyoussef and O. Mounkachi, Phosphorene as a promising anode material for (Li/Na/Mg)-ion batteries: A first-principle study, *Sol. Energy Mater. Sol. Cells*, 2018, **180**, 253–257.
49 K. Tang, L. Fu, R. J. White, L. Yu, M. M. Titirici, M. Antonietti and J. Maier, Hollow Carbon Nanospheres with Superior Rate Capability for Sodium-Based Batteries, *Adv. Energy Mater.*, 2012, **2**, 873–877.
50 D. Aurbach, Z. Lu, A. Schechter, Y. Gofer, H. Gizbar, R. Turgeman, Y. Cohen, M. Moshkovich and E. Levi, Prototype systems for rechargeable magnesium batteries, *Nature*, 2000, **407**, 724–727.
51 M. C. Lin, M. Gong, B. Lu, Y. Wu, D. Y. Wang, M. Guan, M. Angell, C. Chen, J. Yang, B. J. Hwang and H. Dai, An ultrafast rechargeable aluminium-ion battery, *Nature*, 2015, **520**, 324–328.
52 H. Sun, W. Wang, Z. Yu, Y. Yuan, S. Wang and S. Jiao, A new aluminium-ion battery with high voltage, high safety and low cost, *Chem. Commun.*, 2015, **51**, 11892–11895.
53 D. Çakır, C. Sevik, O. Gulseren and F. M. Peeters, Mo_2C as a high capacity anode material: a first-principles study, *J. Mater. Chem. A*, 2016, **4**, 6029–6035.
54 H. R. Jiang, Z. Lu, M. C. Wu, F. Ciucci and T. S. Zhao, Borophene: A promising anode material offering high specific capacity and high rate capability for lithium-ion batteries, *Nano Energy*, 2016, **23**, 97–104.
55 X. He, Y. Zhu and Y. Mo, Origin of fast ion diffusion in super-ionic conductors, *Nat. Commun.*, 2017, **8**, 15893.

